

Superior and Reversible Lithium Storage of SnO₂/Graphene Composites by Silicon Doping and Carbon Sealing

Liyuan Ao, Cong Wu, Xiang Wang, Yanan Xu, Kai Jiang, Liyan Shang, Yawei Li, Jinzhong Zhang, Zhigao Hu,* and Junhao Chu



Cite This: *ACS Appl. Mater. Interfaces* 2020, 12, 20824–20837



Read Online

ACCESS |



Metrics & More



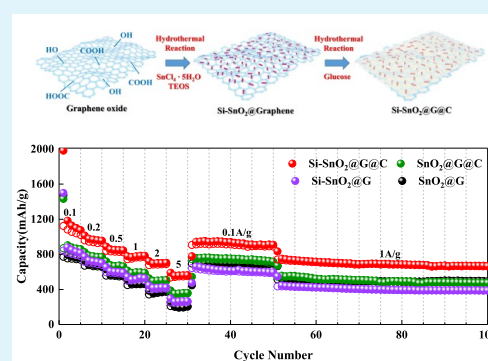
Article Recommendations



Supporting Information

ABSTRACT: The poor cycle stability and reversibility seriously hinder the widespread application of SnO₂ materials as anodes for lithium-ion batteries (LIBs). A novel sandwich-architecture composite of Si-doped SnO₂ nanorods and reduced graphene oxide with carbon sealing (Si-SnO₂@G@C) is engineered and fabricated by a facile two-step hydrothermal process and subsequent annealing treatment, which exhibit not only extraordinary rate performance and ultrahigh reversible capacity but also excellent cycle stability and high electrical conductivity as the anode of LIBs. The Si-doped SnO₂ nanoparticles on the surface of graphene were firmly wrapped in the C-coating and formed a porous sandwich structure, which can efficiently prevent the Sn nanoparticles from aggregation and provide more extra space for accommodating the volume variations and more active sites for reactions. The carbon layer also blocks the direct contact of the SnO₂ nanorods with electrolyte and prevents the graphene nanosheets from the restacking. More importantly, the reversibility of lithiation/delithiation reactions can be remarkably improved by the doping silicon. The doped Si not only accelerates the diffusion of Li⁺ but also brings a significant increase in the specific capacity. As a consequence, the Si-SnO₂@G@C nanocomposite can maintain a high capacity of 654 mAh/g at 2 A/g even after 1200 cycles with negligible capacity loss and excellent reversibility with a Coulombic efficiency retention over 99%, which can be capable of the alternative to commercial graphite anodes. This work provides a new strategy for the reasonable design of advanced anode materials with superior and reversible lithium storage capacity.

KEYWORDS: SnO₂, silicon doping, graphene, carbon sealing, lithium-ion battery



1. INTRODUCTION

The invention of lithium-ion battery (LIBs) opens the process of electronic device portability. Compared with other conventional secondary batteries, lithium-ion batteries are increasingly showing advantages, such as small size, light weight, long life span, excellent environmental protection, and high energy density. Owing to the above characteristics, LIBs are widely applied in power tools, electric vehicles, military equipment, aerospace, and many other fields.^{1–5} Nevertheless, one of the major challenges that restrict its development is to seek alternative electrode materials with high specific capacity to replace the commercial graphite anodes. It has a limited specific capacity of 372 mAh/g and poor rate performance.^{6,7} In recent years, great efforts have been devoted to build hybrid architectures using the materials with high specific capacity for LIB anode, such as mental oxide.^{8,9} As an alternative anode material, SnO₂ with high theoretical capacity (ca. 1493 mAh/g), low cost, and environmental benignity has attracted many explorations on its lithium storage mechanism and practical application.^{10,11} Although it has quite high specific capacity, the drastic capacity fading during the charge/discharge process cannot be neglected, which is due to the huge volume variation

(~300%) and the aggregation of tin particles during the lithiation/delithiation reaction.^{12,13} Moreover, the poor reversibility is also an important factor that hinders its extensive application in the anode materials for LIBs.¹⁴ Therefore, great efforts should be made to overcome these challenges of SnO₂-based materials for their practical applications.

It was reported that constructing nanostructure and compositing with carbon materials could effectively promote the electrochemical performance of SnO₂ materials by buffering the volume expansion and alleviating the diffusion-induced strains during the charge/discharge processes.^{15–20} There have been many successful cases of synthesizing the composites of a carbonaceous matrix, especially graphene, and SnO₂ nanoparticles to overcome the shortcomings of SnO₂ as anode materials of LIBs, such as graphene networks

Received: January 2, 2020

Accepted: April 13, 2020

Published: April 13, 2020



encapsulating hollow SnO₂ nanostructures,²¹ an ultrafine SnO₂/graphene nanocomposite,²² skeleton-structured SnO₂/graphene composite spheres,²³ a sandwiched spherical graphene wrapping SnO₂ nanoparticle composite,²⁴ and so on. Nevertheless, it still needs further amelioration, as the weak interaction and nonintimate contact between graphene nanosheets and SnO₂ nanoparticles are insufficient to restrain the aggregation of Sn particles in the electrode. Besides, driven by van der Waals forces, the graphene nanosheets can easily restack during the drying process, which results in a large charge transfer resistance at the interface.²¹ In addition, in some composites, the SnO₂ particles are directly exposed to the electrolyte, which brings about undesirable side reactions and an unstable interface between SnO₂ and the electrolyte.²⁵ Therefore, it is necessary to design a more subtle structure or introduce other elements to further enhance the energy storage properties of SnO₂–graphene nanostructures.

As we know, among the alternative electrode materials, Si with the highest theoretical capacity of 4200 mAh/g has been studied extensively.^{26,27} However, similar to SnO₂, the large volume change (~400%) caused by the pulverization of silicon particles and thick solid electrolyte interface (SEI) restrict its applications in LIBs.^{28,29} To alleviate these weaknesses, it has attracted extensive attention to fabricate various material structures, such as nanostructured Si materials, nanocomposites, and nanosilicon films, to restrain the volume change of Si during the charge/discharge processes.²⁷ Nevertheless, there have been few reports on improving the electrochemical performances of SnO₂–graphene composites as anode materials of LIBs by doping silicon, which should be a feasible strategy due to the inherent performance advantages of silicon materials. In recent years, several reports have demonstrated that the multiple effects of Si and SnO₂ are beneficial for the lithium storage performance. For instance, Zhou et al. constructed a novel Si@SnO₂ core–shell heterostructure by facile self-assembly of SnO₂ nanowires on silicon hollow nanospheres, which exhibit remarkable synergy in large and reversible lithium storage by the synergy of silicon hollow nanospheres and SnO₂ nanowires.³⁰ Ma et al. also designed a novel hollow structured SnO₂@Si nanosphere, which not only demonstrates high volumetric capacity as anode of LIBs but also prevents aggregation of Sn and confines solid electrolyte interphase thickening.³¹ These Si-based anode materials show excellent electrochemical performance; however, they still have some shortcomings like poor cycle stability and electrical conductivity.

Herein, according to the above discussion, a novel sandwich-architecture composite of Si-doped SnO₂ nanorods and reduced graphene oxide with carbon sealing (Si-SnO₂@G@C) is designed and fabricated by a two-step hydrothermal process and subsequent annealing treatment. The electrochemical performance of Si-SnO₂@G@C has been significantly enhanced by doping silicon and sealing carbon layer. The Si-doped SnO₂ nanoparticles on the surface of graphene were firmly wrapped in the C-coating and formed a sandwich structure, which can efficiently prevent the Sn nanoparticles from aggregation by obstructing the diffusion of Sn atoms. The carbon layer also blocks the direct contact of the SnO₂ nanorods with electrolyte and prevents the graphene nanosheets from restacking. What is more, the reversibility of lithiation/delithiation reactions is remarkably improved by doping silicon. Additionally, the doped Si not only generates Li⁺ conductive Li₄SiO₄ during lithiation process but also

decreases the defects in the carbon matrix and indeed accelerates the diffusion of Li⁺. Besides, the doped Si can make the structure more wrinkled and porous, providing more extra space for accommodating the volume variations and more active sites for reactions. Therefore, it can lift the specific capacity due to the adsorption of extra lithium ions in the more wrinkled structure. As a consequence, the Si-SnO₂@G@C nanocomposite exhibits extraordinary rate performance, ultra-high specific capacity, excellent cycle stability, and high electrical conductivity as the anode of LIBs.

2. EXPERIMENTAL SECTION

Materials Preparation. Si-SnO₂@G@C was prepared via a two-step hydrothermal process and subsequent annealing treatment. Graphene oxide (GO) was synthesized by using a modified Hummers' method from graphite nanosheets. Typically, SnCl₄·5H₂O (0.01 M) was dissolved in a 50 mL GO colloidal solution under magnetic stirring. Then 50 μL of tetraethyl orthosilicate (TEOS) was dispersed in the above pseudo-solution by stirring for another 30 min and ultrasound treatment for 1 h. 10 mL of urea solution (2.5 M) and 5 mL of HCl were added to the mixture by dropwise addition and quick transfer, respectively. Next, the uniform and stable colloidal solution in chocolate color was transferred into a 100 mL Teflon-lined stainless steel autoclave and hydrothermally treated at 200 °C for 24 h. After cooling to room temperature, 0.03 mol of glucose was added to the autoclave for the second hydrothermal reaction, which was kept at 180 °C for 1 h. The black product was collected, washed with DI water and ethanol by centrifugation for several times, and dried at 80 °C overnight. Finally, the Si-SnO₂@G@C was obtained after annealing in Ar at 600 °C for 2 h. The Si-SnO₂@G was gained without the second step hydrothermal treatment. In addition, SnO₂@G and SnO₂@G@C samples were also produced for comparison using the above method without the addition of TEOS only. Also, the Si-SnO₂@G@C composites with 10, 100, and 200 μL of TEOS were prepared and named Si-SnO₂@G@C-1, Si-SnO₂@G@C-2, and Si-SnO₂@G@C-3, respectively.

Materials Characterization. Scanning electron microscopy (SEM) images were obtained from a PHILIPS XL30TMP. The high-resolution transmission electron microscopy (HRTEM) and elemental mapping studies were measured by using a TALOS F200X at an accelerating voltage of 200 kV. X-ray diffraction (XRD) analyses were performed on a high-resolution powder X-ray diffractometer with Cu Kα radiation (λ = 1.5418 Å) over a 2θ range from 10° to 80°. Raman spectra were conducted on a Jobin-Yvon LabRAM HR Evolution spectrometer equipped with a 532 nm laser. X-ray photoelectron spectroscopy (XPS) was characterized by using a RBD upgraded PHI-5000C ESCA system (PerkinElmer) with Mg Kα radiation (hν = 1253.6 eV). Thermogravimetric analysis (TGA) was performed in air with a heating rate of 10 °C/min over a temperature range from 30 to 900 °C.

Electrochemical Measurement. The coin-type 2025 cells were employed for the electrochemical performance test. The electrodes were fabricated via a conventional slurry based method using an *N*-methyl-2-pyrrolidone (NMP) slurry with 70 wt % active materials, 20 wt % acetylene black, and 10 wt % poly(vinylidene fluoride) (PVDF) binder. The homogeneous slurry was pasted onto a clean copper foil and dried at 80 °C overnight in a vacuum oven. The mass loading of active material in electrode was about 0.8–1.2 mg/cm². The coin cells were assembled in an Ar-filled glovebox with metallic lithium as counter electrode and Celgard 2400 polypropylene film as separator. The electrolyte was formulated in a solution of LiPF₆ (1 M) in a 1:1:1 in volume ratio of ethylene carbonate, dimethyl carbonate, and diethyl carbonate. The galvanostatic discharge–charge (GCD) measurements were performed on a Land CT 2001A battery tester in a voltage window of 0.01–3 V (vs Li/Li⁺). The cyclic voltammetry (CV) test and electrochemical impedance spectroscopy (EIS) were examined by using a CHI-660D electrochemical workstation.

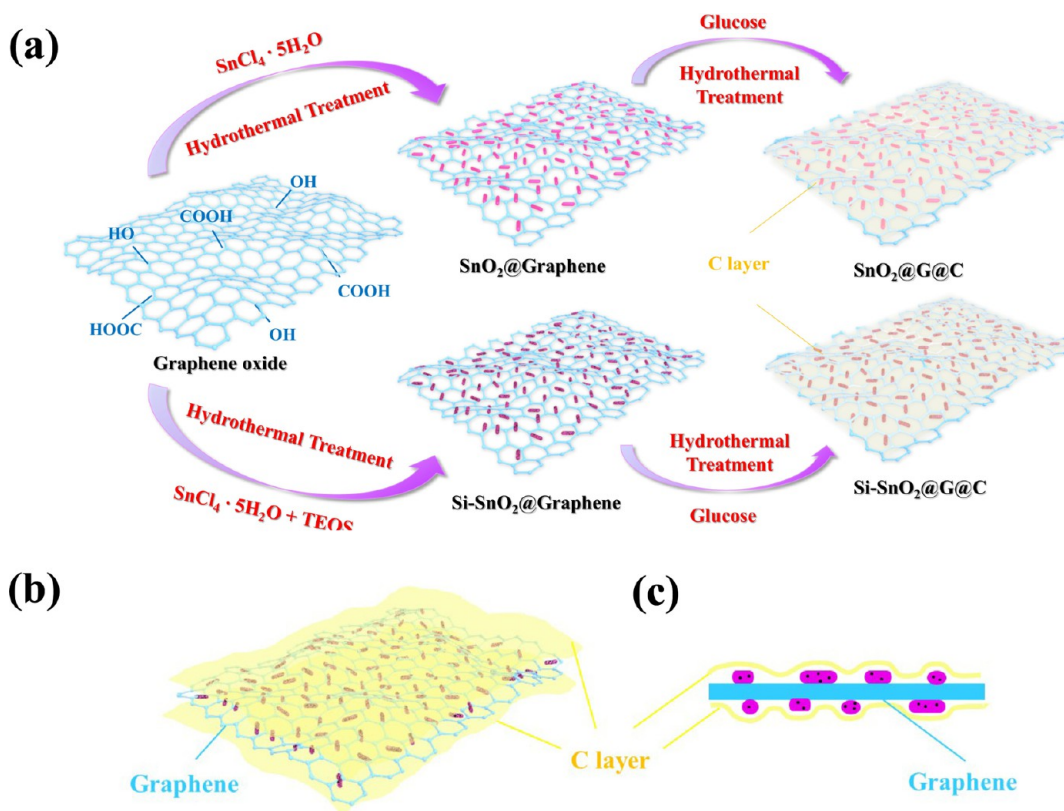


Figure 1. (a) Schematic illustration for the preparation of the sandwich-architecture SnO_2 @G@C and Si-SnO_2 @G@C nanocomposites. (b) Structural diagram and (c) cross-sectional diagram of the Si-SnO_2 @G@C nanocomposites.

3. RESULTS AND DISCUSSION

Figure 1 graphically demonstrated the integrated synthetic routes of sandwich-architecture Si-SnO_2 @G@C and SnO_2 @G@C. First, the GO nanosheets obtained through Hummers' method were dispersed into single layer nanosheets by ultrasonic treatment. The $\text{SnCl}_4 \cdot 5\text{H}_2\text{O}$ and TEOS were used as tin and silicon precursors, which were attracted to the GO surface by hydrogen bonding or π - π interactions with functional groups by stirring and ultrasound. During the first step hydrothermal process, the Si-SnO_2 (SnO_2) nanorods were obtained and attached to the surface of the reduced graphene oxide (rGO) nanosheets. Meanwhile, the GO was reduced to rGO. Then, the glucose was used as carbon precursor to conduct the carbon coating process. The conditions of 180 °C and 1 h are necessary to form a uniform and ultrathin carbon layer, which can cover the upper and lower surfaces of the Si-SnO_2 @G (SnO_2 @G) composite. The final sandwich-architecture Si-SnO_2 @G@C (SnO_2 @G@C) was produced after the annealing process, which reduced the defects inside the composite and made the crystallization more favorable and the structure more stable. The C-coated sandwich structure can efficiently prevent aggregation of Sn nanoparticles and restacking of graphene nanosheets as well as block the direct contact of the SnO_2 nanorods with electrolyte.

The morphology and the microstructure of the four samples were characterized by using the SEM and TEM images, as shown in Figures 2 and 3 (Figures S1 and S2), respectively. All the four samples exhibit visible nanosheet structures. The surface of the SnO_2 @G is the smoothest of the four composites; however, the Si-SnO_2 @G@C shows the most conspicuous laminated structure. Upon comparison of Figure

2a with Figure 2c or Figure 2b with Figure 2d, it can be inferred that the doped Si makes the structure more wrinkled and porous. Because of the flexible peculiarity of graphene and their strong π - π interaction, the samples without Si are easy to be crumpled into large particles (Figure 2a,b and Figure S1a-h). It is reported that the doped Si can improve the mechanical rigidity of the SnO_2 @G nanosheets.³² Therefore, the nanosheets can readily interconnect with each other without aggregation, which can result in more wrinkled and porous three-dimensional (3D) structure. Besides, the effect of the doped Si on the morphology is more obvious from Figure 2a,c. The surface of SnO_2 @G is smooth with visible grains, while clear folds can be seen on the surface of Si-SnO_2 @G without granular sensation. The folds can act as electrolyte reservoir to reduce ion transport resistance. In addition, Figure 2d shows that the ultrathin nanosheets are interconnected with each other to form 3D porous structure with carbon coating. However, the structure is not distinct for the samples without carbon coating due to the restacking of graphene nanosheets during drying and annealing. The carbon coating inhibits the volume expansion of Si-SnO_2 nanorods and ensures the stability of the composite structure during the cycling. Therefore, it can be concluded that the stable porous sandwich structure must be achieved by the synergy of silicon doping and carbon coating. This favorable 3D porous microstructure of the Si-SnO_2 @G@C provides more extra space for accommodating the volume variations and more active sites for reactions. Besides, it can improve the interfacial contact and promote the diffusion of Li^+ . To further reveal the details and the inner nanostructures of the Si-SnO_2 @G@C nanocomposite, TEM and HRTEM characterizations have been

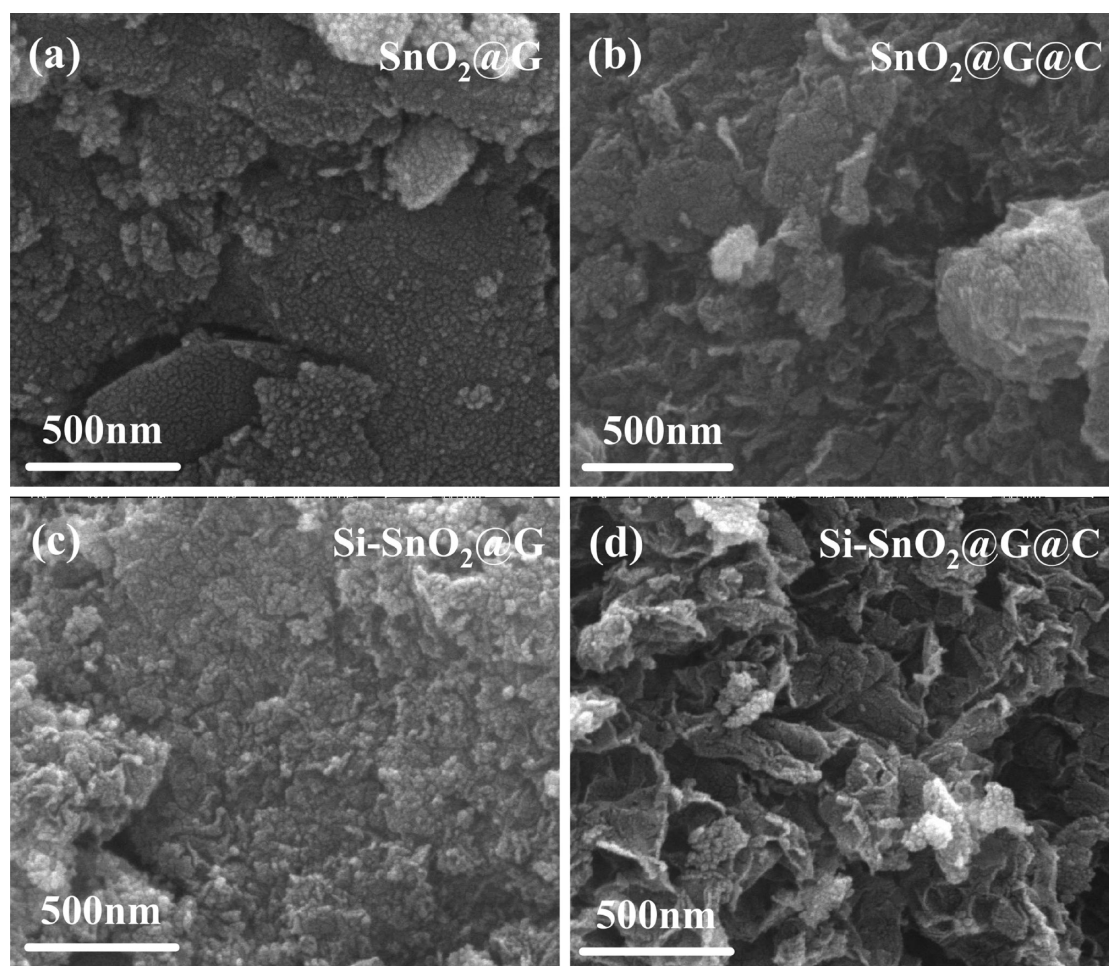


Figure 2. (a–d) High-magnification SEM images of SnO₂@G, SnO₂@G@C, Si-SnO₂@G, and Si-SnO₂@G@C, respectively.

conducted. Figure 3 and Figure S2 present the rice-granular Si-SnO₂ nanorods with a length of 10–20 nm and a diameter of around 5 nm evenly and densely distributed on the graphene nanosheet. From Figure 3c,d the graphene and the ultrathin C-coating layer can be clearly distinguished, which indicate the sandwich architecture of the Si-SnO₂@G@C. The HRTEM images in Figure 3d and Figure S2 further reveal that the well-dispersed nanocrystallites have nonuniform shapes, and the observed lattice spacing of 0.334 nm corresponds to the (110) planes of tetragonal SnO₂. The STEM image and its corresponding EDS elemental mapping are exhibited in Figure 3e–j to further demonstrate the distribution of SnO₂ nanoparticles and silicon element. Figure 3f indicates that the tin element is completely crystallized to form SnO₂ nanorods, which are sealed in the carbon layer. The distributions of oxygen and silicon are similar to that of tin, which suggests that the silicon is doped in the SnO₂ nanoparticles forming Si-SnO₂ nanorods.

X-ray diffraction (XRD) analysis was employed to study the crystal structures and phase transformation of the four samples. The results are exhibited and compared in Figure 4a. For all the four samples, the typical diffraction peaks at $2\theta = 26.6^\circ, 33.9^\circ, 37.9^\circ, 39.1^\circ, 51.8^\circ, 54.7^\circ, 57.9^\circ, 61.9^\circ, 64.8^\circ, 66.0^\circ, 71.3^\circ, \text{ and } 78.7^\circ$ could be indexed to the (110), (101), (200), (111), (211), (220), (002), (310), (112), (301), (202), and (321) diffraction planes of the tetragonal SnO₂ with a *P42/mnm* space group (JCPDS No. 41-1445), respectively. As for

SnO₂@G, all the diffraction peaks can correspond to them. For other three samples, however, the weak diffraction peaks at $2\theta = 30.6^\circ, 32.0^\circ, 43.9^\circ, 44.9^\circ, 55.3^\circ, 62.5^\circ, 63.8^\circ, 64.6^\circ, 72.4^\circ, 73.1^\circ \text{ and } 79.5^\circ$ could be indexed to the (200), (101), (220), (111), (301), (112), (400), (321), (420), (411), and (312) diffraction planes of cubic phase Sn (JCPDS No. 65-2631), respectively. These results demonstrate that the Sn⁴⁺ is crystallized to form rutile-type SnO₂ crystals after the hydrothermal treatment. The appearance of the Sn peaks may be due to the fact that a very small amount of SnO₂ is reduced to Sn during the annealing process. The effect on the entire composite can be negligible. It should be pointed out that there are no peaks indexed to Si or SiO_x, which can be ascribed to the formation of amorphous SiO_x and the low content of doped Si. Additionally, to investigate the change in the carbon matrix by doping Si, Raman spectroscopy using a 532 nm laser as the excitation source was adopted. As shown in Figure 4b, two obvious peaks corresponding to the D-band (*k*-point phonons of A_{1g} symmetry) and the G-band (E_{2g} phonon of C sp² atoms) of carbon material can be found in the Raman spectra of all the four composites at 1342 and 1597 cm⁻¹, respectively.³³ As for Si-SnO₂@G and Si-SnO₂@G@C, there is a sharp peak at 478 cm⁻¹, which can be indexed to the amorphous SiO_x with a phonon confinement effect or a masking effect of the graphene and C-coating.³⁴ It is well-known that the ratio of the intensities of the D-band to the G-band (*I_D/I_G*) is an indicator of the degree of graphitic disorder.

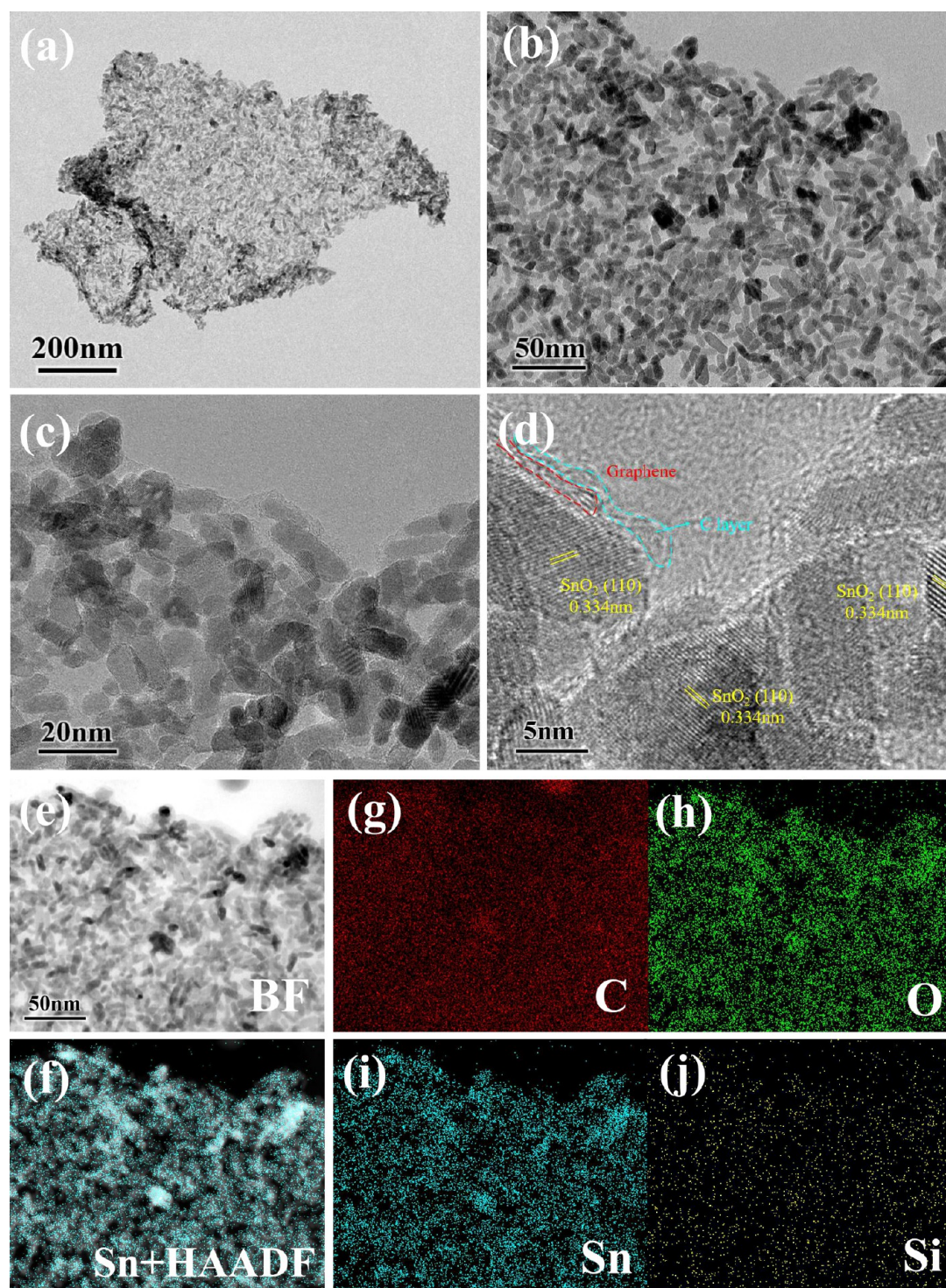


Figure 3. (a–c) TEM and (d) HRTEM images of Si-SnO₂@G@C. (e) STEM image of Si-SnO₂@G@C composite and the corresponding elemental mapping images of (f) Sn + HAADF, (g) C, (h) O, (i) Sn, and (j) Si.

The I_D/I_G values of Si-SnO₂@G and Si-SnO₂@G@C were calculated to be 0.99 and 1.03, respectively, which are lower than the composites without the Si doping. Also, the values of the samples with C-coating are lower, indicating that the defects of carbon matrixes decrease on account of the doped Si and the introduction of partially graphitizing mesoporous carbon around the graphene nanosheets.³⁵ It can thereby accelerate the diffusion of the lithium ions.

In addition, Figure 4c shows the thermogravimetric analysis (TGA) curves to determine the contents of C for the four samples. Because the content of SiO_x and Sn reduced by SnO₂ is very low, the influence of the oxidation of SiO_x and Sn can be neglected. The graphene approximately accounts for 26.8 wt % of Si-SnO₂@G and 29.2 wt % of SnO₂@G. As for Si-SnO₂@G@C and SnO₂@G@C, the total contents of C are estimated as 32.1 and 38.1 wt %. Thus, the contents of C-coating can be roughly estimated as 5.3 and 8.9 wt %, respectively.

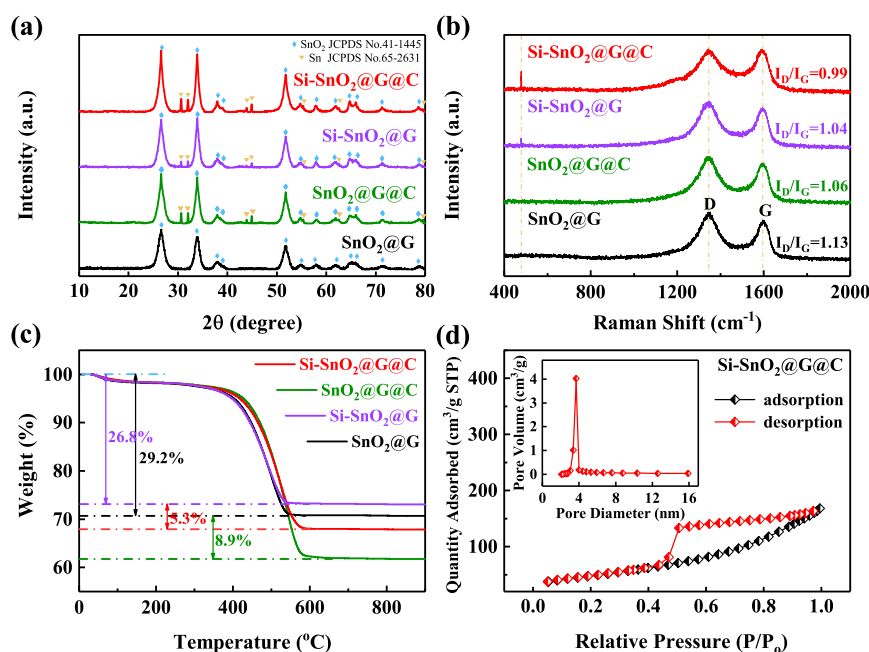


Figure 4. (a) XRD patterns, (b) Raman spectra, and (c) TGA curves of the as-prepared SnO₂@G, SnO₂@G@C, Si-SnO₂@G, and Si-SnO₂@G@C. (d) N₂ adsorption–desorption isotherms of Si-SnO₂@G@C composite; the inset shows the corresponding pore size distribution curve.

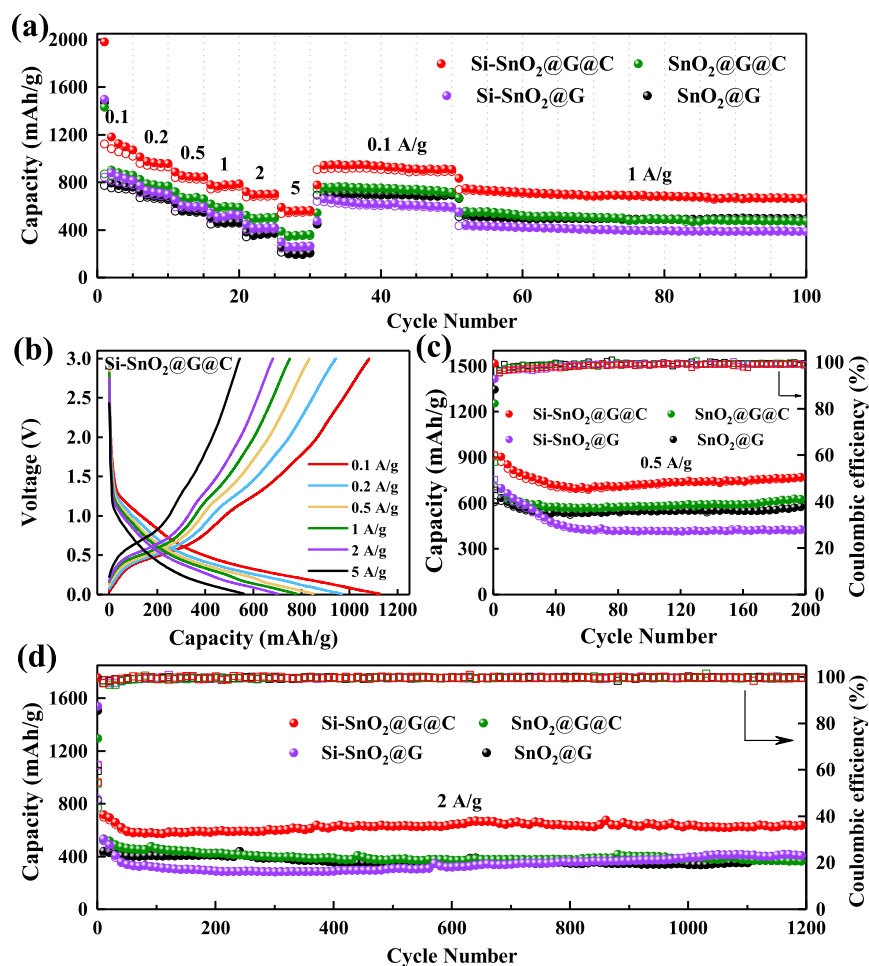


Figure 5. (a) Rate performance of the four composite electrodes at various current densities. (b) GCD profiles of Si-SnO₂@G@C at the increasing discharge current density from 0.1 to 5.0 A/g. Cycling performance and Coulombic efficiency of the as-prepared samples cycled at (c) 0.5 A/g for 200 cycles and (d) 2 A/g for 1200 cycles, at 0.1 A/g for the first five cycles.

respectively. Moreover, nitrogen adsorption–desorption isotherms were measured for all the four samples, and the results of the Si-SnO₂@G/C composite are shown in Figure 4d. A mesoporous structure is confirmed, and it shows a type IV adsorption–desorption pattern.³⁶ The corresponding pore size distribution curve shown in the inset indicates that the micropores are uniformly distributed around 3.7 nm, which is in accordance with the SEM and TEM results. The Brunauer–Emmett–Teller (BET) surface area and the total volume in pores of SnO₂@G, Si-SnO₂@G, SnO₂@G/C, and Si-SnO₂@G/C are 204.4 m² g⁻¹/0.1948 cm³ g⁻¹, 203.7 m² g⁻¹/0.2516 cm³ g⁻¹, 216.9 m² g⁻¹/0.2303 cm³ g⁻¹, and 169.1 m² g⁻¹/0.2161 cm³ g⁻¹, respectively. All the samples have quite large BET surface area and relatively large total volume in pores (Figure S3), which can competently buffer the tremendous volume expansion of SnO₂ nanorods during the lithiation/delithiation process. The BET surface is evidently reduced by the synergistic effect of C-coating and Si doping, which could reduce the consumption of electrolyte caused by surface reactions.

To further analyze the composition and the valence state of the Si-SnO₂@G/C composite, X-ray photoelectron spectroscopy (XPS) was performed. Four typical peaks at 284.8, 487.4, 495.8, and 531.3 eV can be observed in the XPS overall spectra (Figure S4a), which correspond to C 1s, Sn 3d_{5/2}, Sn 3d_{3/2}, and O 1s, respectively. However there are no obvious peaks belonging to Si because of the lower doping. The high-resolution Sn 3d spectrum of Si-SnO₂@G/C (Figure S4b) shows two well-proportioned peaks at 495.8 and 487.4 eV, which are related to Sn 3d_{3/2} and Sn 3d_{5/2}, respectively. It is found by the fitting analysis that the peaks entirely belong to the Sn⁴⁺, which is a further proof of the SnO₂ crystals.³⁷ Note that there are no peaks belonging to Sn⁰ because there were no metallic Sn impurities within the range of samples that XPS can detect due to the small amount of the test sample and the low content of the impurity Sn. As shown in Figure S4c, the broad peak in the high-resolution O 1s spectrum could be fitted into three peaks at 531.1, 531.6, and 532.8 eV, which are in accord with Sn–O, Si–O, and C–O bonds, respectively.³⁸ The existence of an Si–O bond provides evidence to the doped Si. As for the deconvoluted C 1s spectrum, it could be fitted into four peaks associated with C–C (289.6 eV), C–O (286.1 eV), and O–C=O bonds (284.8 eV).³⁹ The peaks of C–O and O–C=O bonds are quite weak, which may be because the oxygen-containing functional groups are removed by the high-temperature thermal treatment in argon. The Si 2p spectrum shows two fitting peaks located at 103.7 and 102.8 eV, which are assigned to Si⁴⁺ and Si³⁺.⁴⁰ Thus, it can be concluded that the doped silicon is present in the form of amorphous SiO_x, which is consistent with the Raman spectra. The atomic concentrations of the elements in Si-SnO₂@G/C and SnO₂@G/C determined by the XPS analysis are presented in Figure S4f. Consistent with the thermogravimetric analysis, the atomic content of C in SnO₂@G/C is slightly higher than Si-SnO₂@G/C, which can be considered as a result of the effect of doped silicon on the carbon coating. In addition, the atomic concentration of Si is only 0.45% for the Si-SnO₂@G/C composite, and that of Sn is 7.75%.

The electrochemical performance of the four composites as anode materials for a lithium-ion battery is first evaluated by galvanostatic charge/discharge (GCD) measurements in half-cells. The rate capacity and cycle stability of the sample electrodes were tested in the voltage range of 0.01–3.0 V (vs

Li⁺/Li), as shown in Figure 5. Figure 5a illustrates the rate capacity of the five sample electrodes at different current densities from 0.1 to 5 A/g and then back to 0.1 and 1 A/g, respectively. It can be seen that the rate performance of the Si-SnO₂@G/C electrode shows a significant improvement compared to other three samples, which exhibits both higher reversible capacity and higher capacity retention. The Si-SnO₂@G/C electrode delivers reversible capacity of 1127, 968, 851, 780, 704, and 564 mAh/g at 0.1, 0.2, 0.5, 1, 2, and 5 A/g, respectively. After 50 cycles, it returns back to 913 mAh/g at 0.1 A/g. Also, it remains at 670 mAh/g even after the next 50 cycles at 1 A/g, demonstrating its outstanding reversibility and cycle stability. Moreover, the Si-SnO₂@G/C electrode has a tremendously high initial discharge capacity up to 1981 mAh/g at 0.1 A/g, which is much higher than the theoretical capacity of SnO₂ and most previous reports in SnO₂-based materials as anode materials of LIBs. Besides, the rate capacities of other three electrodes are not much different, which indicates that the improvement in rate performance must rely on the combination of silicon doping and carbon cladding. It is because the sandwich structure cannot be wrinkled and porous without the doped Si, which can provide more extra space for accommodating the volume variations and more active sites for reactions. Without the carbon layer, however, the SnO₂ nanorods will directly contact with the electrolyte and the graphene nanosheets will restack during the drying process. Thereby, the structure will be instability during the lithiation/delithiation reactions, resulting in the capacity reduction especially at high current densities. To further analyze its rate performance, the charge–discharge curves of the Si-SnO₂@G/C electrode at different current density are displayed in Figure 5b. There is no obvious hysteresis growth in charge–discharge plateaus even at a high current density of 5 A/g, which proves its superlative electronic/ionic transport characteristics. To further characterize the role of Si in the Si-SnO₂@G/C electrode, the electrochemical performance of the composite electrodes with different silicon content is also evaluated by GCD measurements in half-cells. The rate performance of the composite electrodes is shown in Figure 5S, indicating that the doping amount of silicon (50 μL of TEOS) for the Si-SnO₂@G/C electrode has the optimum rate performance. It is found that the skimpy silicon doping (Si-SnO₂@G/C-1 with 10 μL of TEOS added) cannot increase the specific capacity of SnO₂@G/C. That may be because the introduction of trace impurities does not show the beneficial effect of silicon but will destroy the properties of the original composite. The excessive silicon doping (Si-SnO₂@G/C-3 with 200 μL of TEOS added) can increase the initial capacity of SnO₂@G/C. However, the specific capacity is decreased significantly as the excessive silicon doping exacerbate the volume change during cycling. The 100 μL TEOS addition can slightly improve the rate performance, which means the beneficial effect of the doped Si on the electrochemical performance of SnO₂@G/C anode. However, the capacities of Si-SnO₂@G/C-2 and Si-SnO₂@G/C-3 are much smaller than that of Si-SnO₂@G/C, which is because excessive silicon doping can make the mechanical rigidity of the nanosheets too strong to form an optimal porous structure.

The stabilities of the four anode materials during the charge/discharge process at different current densities are compared in Figure 5c,d. Figure 5c shows the galvanostatic cyclability at 0.5A/g in the voltage range of 0.01–3.0 V (vs Li⁺/Li) for 200 cycles. The four samples show a capacity decline within the

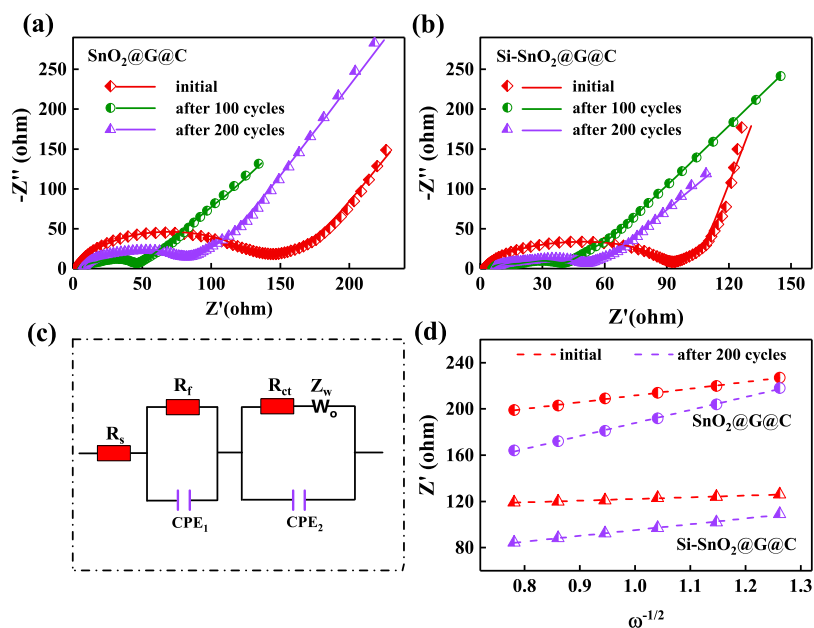


Figure 6. Electrochemical impedance spectra (symbol) and the fitting curves (line) of the (a) $\text{SnO}_2@\text{G}@\text{C}$ and (b) $\text{Si-SnO}_2@\text{G}@\text{C}$ for before and after 100 and 200 cycles. (c) Equivalent circuit used in EIS. (d) Relationship plots between Z' and $\omega^{1/2}$ in the low-frequency range of $\text{SnO}_2@\text{G}@\text{C}$ and $\text{Si-SnO}_2@\text{G}@\text{C}$.

first 40 cycles as a result of the SEI fluctuation and electrolyte decomposition. For $\text{Si-SnO}_2@\text{G}@\text{C}$, the specific capacity starts to increase after 60 cycles, which can be attributed to the excellent pseudocapacitive effect. However, the capacities of the other three samples remain steady in the 40–200 cycles. The samples with Si doping have notably more capacity fading than the other two, which can be ascribed to the thicker solid electrolyte interface. However, with carbon coating and synergistic effect of Si and C, a discharge capacity of 772 mAh/g is retained after 200 cycles for the $\text{Si-SnO}_2@\text{G}@\text{C}$, which is much higher than other samples. In addition, the curves of the $\text{SnO}_2@\text{G}@\text{C}$ and $\text{SnO}_2@\text{G}$ electrode are almost same, further proving the synergistic effect of Si and C on electrochemical performance. Furthermore, the Coulombic efficiency of the $\text{Si-SnO}_2@\text{G}@\text{C}$ electrode is the highest of the four samples at 0.5 A/g, which is 60.2% initially and increases to 91.7% at the second cycle and then maintains over 97% after 15 cycles. To further investigate the long-term cycling performance of the four electrodes, another galvanostatic cyclability test was conducted at a high current density of 2 A/g (0.1 A/g for the first five cycles), as shown in Figure 5d. Unsurprisingly, the $\text{Si-SnO}_2@\text{G}@\text{C}$ electrode shows an optimal cyclability and a highest capacity of 654 mAh/g even after 1200 cycles, which shows a 93.4% retention of the initial capacity and a Coulombic efficiency retention over 99%. The capacity curves of the $\text{SnO}_2@\text{G}@\text{C}$ and $\text{SnO}_2@\text{G}$ electrode are also steady with a little decline; however, the capacity of the $\text{Si-SnO}_2@\text{G}$ electrode exhibits a trend from severe decline to slowly increase to stability, which can be due to the effect of the doped Si on the electrochemical performance of $\text{SnO}_2@\text{G}$ composite. Particularly, the specific capacity of $\text{Si-SnO}_2@\text{G}$ is even lower than that of $\text{SnO}_2@\text{G}$ in the 20–600 cycles in Figure 5d and the 20–200 cycles in Figure 5c. That is because the structure of $\text{Si-SnO}_2@\text{G}$ is also instable and has even larger volume expansion during the cycle process due to the property of Si. Also, the doped Si leads to a thicker solid electrolyte interface, which causes a more obvious

capacity fading in the first several cycles. However, the initial discharge capacity and Coulombic efficiency of $\text{Si-SnO}_2@\text{G}$ are higher than those of $\text{SnO}_2@\text{G}$, as shown in Figure 5a,c,d. It can be demonstrated that the Si doping has a positive effect on the electrochemical performance.

To further study the effect of silicon doping on lithium ion diffusion, an electrochemical impedance spectroscopy (EIS) measurement was performed with the new cells, the cells after the rate test for 100 cycles, and the cells after 200 galvanostatic charge/discharge cycles at the current density of 0.5 A/g for $\text{SnO}_2@\text{G}@\text{C}$ and $\text{Si-SnO}_2@\text{G}@\text{C}$. As shown in Figure 6a,b, the Nyquist plots contain a semicircle in the high-frequency region connected with the transfer resistance of the lithium ion through the SEI film (R_f). Another semicircle in the medium-frequency region is related to the charge transfer resistance (R_{ct}) at the electrode interface and a slope in the low-frequency region. It can be assigned to the Warburg impedance (Z_w), which is related to diffusion process of lithium ion.⁴¹ The EIS spectra could be well fitted by using the equivalent circuit in Figure 6c, where R_s is regarded as the internal resistance and leads to the intercept of the high-frequency semicircle on the Z' -axis. The fitting values of R_s , R_f and R_{ct} are shown in Table S1. Before cycling, the fitting values of R_f and R_{ct} of $\text{Si-SnO}_2@\text{G}@\text{C}$ are 52.0 and 29.9 Ω , respectively, which are both smaller than that of $\text{SnO}_2@\text{G}@\text{C}$ (127.3/81.4 Ω). It means that the transfer of a lithium ion and an electron at the electrode/electrolyte interface is much faster for $\text{Si-SnO}_2@\text{G}@\text{C}$. The values of R_f and R_{ct} of the two composites significantly decrease after 100 cycles due to the ultrafine nanocrystals formed during the cycling. After 200 cycles, however, the values of the fitted R_f and R_{ct} increase slightly for $\text{SnO}_2@\text{G}@\text{C}$. Nevertheless, they do not considerably change for $\text{Si-SnO}_2@\text{G}@\text{C}$. It further demonstrates that the doped Si can efficiently improve the stability of internal structure and electrochemical performance. Furthermore, the resistance (Z') in the low-frequency region related to the lithium-ion transportation is evidenced by the linear response to $\omega^{1/2}$, which can be

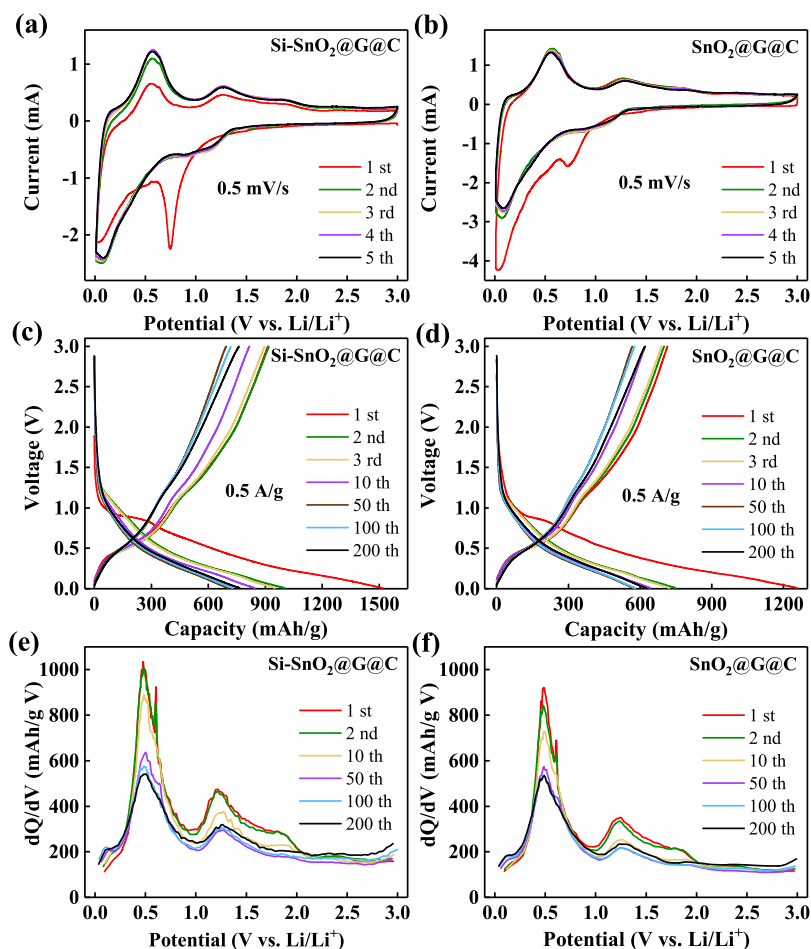


Figure 7. CV curves of (a) Si-SnO₂@G@C electrode and (b) SnO₂@G@C electrode at a scan rate of 0.5 mV/s in the range of 0.01–3.0 V vs Li/Li⁺. The GDC profiles of (c) Si-SnO₂@G@C and (d) SnO₂@G@C for the 1st, 2nd, 3rd, 10th, 50th, 100th, and 200th cycles at 0.5 A/g. The differential charge capacity curves of (e) Si-SnO₂@G@C and (f) SnO₂@G@C at the 1st, 2nd, 10th, 50th, 100th, and 200th cycles at 0.5 A/g.

described as $Z' = R_{ct} + R_{el} + \sigma\omega^{1/2}$, where R_{ct} , R_{el} , and ω are the charge transfer resistance, electrolyte resistance, and angular frequency, respectively. The parameter σ is the Warburg factor corresponding to the slope of the curve in Figure 6d, which is related to the lithium ion diffusion coefficient.³⁷ According to the results, the initial value of ω for Si-SnO₂@G@C is smaller than that of SnO₂@G@C, which increases slightly after 200 cycles. It can be inferred that Si-SnO₂@G@C has a higher lithium ion diffusion coefficient, and the diffusion of Li⁺ is hindered slightly during the charge/discharge cycles as compared to the case of SnO₂@G@C.

Cyclic voltammetry (CV) was used to explore the electrochemical reaction in detail and confirm the effect on the lithiation/delithiation reaction of Si addition at a sweep rate of 0.5 mV/s from 0.01 to 3.0 V vs Li/Li⁺. Figure 7a,b illustrates the first five cycles of the CV curves of Si-SnO₂@G@C and SnO₂@G@C, respectively. For the initial cathodic (lithium insertion) scan, a quite distinct reduction peak at around 0.75 V can be found for both the two electrodes, corresponding to the formation of Li₂O. It disappears in the subsequent cycles as a result of the formation of the SEI layer on the surface of the active material.⁴² The peak of Si-SnO₂@G@C is much sharper than that of SnO₂@G@C, suggesting an increase of the initial capacity for doping Si to the SnO₂@G@C. It can be attributed to the reaction of SiO_x with Li⁺ ($\text{SiO}_x + \text{Li}^+ + \text{e}^- \rightarrow \text{Si} + \text{Li}_2\text{O} + \text{Li}_4\text{SiO}_4$)³⁸ and the enhancement of the

reduction of SnO₂ to Sn ($\text{SnO}_2 + 4\text{Li}^+ + 4\text{e}^- \rightarrow \text{Sn} + 2\text{Li}_2\text{O}$). Also, the peak near 0 V in the CV curves of the two samples corresponds to the formation of Li_{4.4}Sn alloys ($\text{Sn} + 4.4\text{Li}^+ + 4.4\text{e}^- \leftrightarrow \text{Li}_{4.4}\text{Sn}$).⁴³ In the second to the fifth cycle, the visible peak is divided into two peaks at around 0.11 and 0.34 V, which represent the alloying reaction of Li_xSn. Besides, there are another two weak peaks at about 1.14 and 0.86 V, which can be linked with the conversion of SnO₂ to SnO/Li₂O and SnO to Sn/Li₂O, respectively. All of the four reduction peaks can correspond to the oxidation peaks in anodic (lithium deintercalation) scan, revealing the reversibility of the two electrodes. Besides, the broad peak at 0.57 V and the small peak at 0.64 V can be related to the multiple dealloying reaction of Li_xSn for Li ion extraction in the SnO₂@G@C electrode. However, the two oxidation peaks also appear and are sharper in the Si-SnO₂@G@C electrode than in the SnO₂@G@C electrode, which may be due to the overlap of oxidation peaks corresponding to the formation of the Li–Si alloy ($\text{Si} + \text{Li}^+ + \text{e}^- \leftrightarrow \text{Li}_x\text{Si}$) and the Li–Si alloy ($\text{Sn} + \text{Li}^+ + \text{e}^- \leftrightarrow \text{Li}_x\text{Sn}$). It further demonstrates that the lithium storage capacity of Si-SnO₂@G@C could be enhanced by the doped Si. Nevertheless, the two weak peaks at 1.26 and 1.87 V match with the oxidation of Sn to SnO and SnO to SnO₂, respectively. Additionally, the CV curves of the two electrodes in the second to fifth cycle are highly coincident, demonstrating that the electrochemical reactions in both the

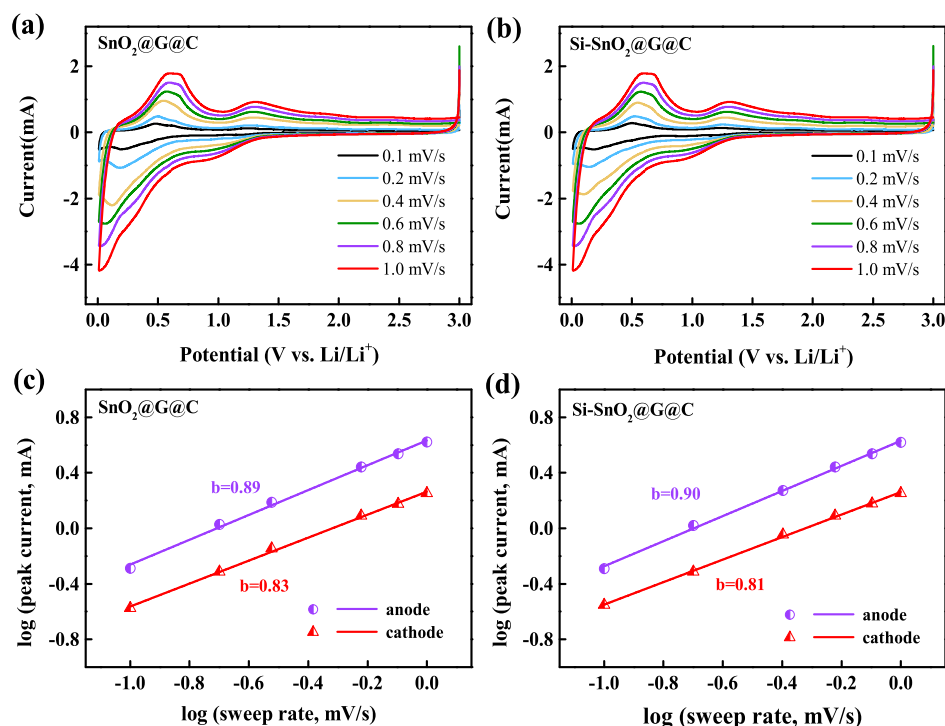


Figure 8. CV curves at various rates from 0.1 to 1 mV/s of (a) the Si-SnO₂@G@C electrode and (b) the SnO₂@G@C electrode. The fitted specific anodic/cathodic peak current for determining the b value of (c) Si-SnO₂@G@C and (d) SnO₂@G@C.

Si-SnO₂@G@C and SnO₂@G@C electrodes are greatly reversible. What is more important, as compared to the SnO₂@G@C electrode, all the redox peaks of Si-SnO₂@G@C are more distinct, confirming the improvement of the reversibility during the lithiation/delithiation process by the doped Si.

The electrochemical reactions found in CV curves are consistent with the plateaus in galvanostatic voltage–capacity curves at a current density of 0.5 A/g (Figure 7c,d). It can be observed that the 1st to 3rd and the 50th to 200th charge–discharge curves show good superposition, especially for Si-SnO₂@G@C. It further reveals the favorable cycle stability of Si-SnO₂@G@C. To intuitively analyze the durability differences of conversion reaction between these two composites, the differential charge capacity plots (DCPs) are displayed in Figure 7e,f. Four typical peaks at 0.57, 0.64, 1.26, and 1.87 V correspond to the multiple dealloying reaction of Li_xSn, oxidation reactions of Sn and SnO, consistent with the CV results exactly. The peaks of Si-SnO₂@G@C are obviously sharper than that of SnO₂@G@C, especially for the dealloying peaks in 0.5–0.7 V. This could be attributed to the overlap of the oxidation peaks, which are responsible for the dealloying reaction of Li_xSn and Li_xSi ($\text{Si} + x\text{Li}^+ + xe^- \leftrightarrow \text{Li}_x\text{Si}$). It demonstrates the extra lithium storage capacity induced by the doped Si. Moreover, the intensity of the peaks gradually decreases with increasing the cycle times, indicating that the reversibility of the conversion reaction reduces during the cycle process. In addition, it is well-known that Li₄SiO₄ is a fast conductor of Li⁺, and the diffusion of lithium ions in Si-SnO₂@G@C composite is accelerated by the Li₄SiO₄ produced from activation of SiO_x. As a consequence, the lithiation/delithiation of Li–Sn became more reversible by the doped Si.

Note that the reversible capacity of the Si-SnO₂@G@C electrode has exceeded the theoretical value, which could be attributed to the capacitive mechanism for energy storage,

including diffusion-control capacity and surface pseudocapacitance. Figure 8 shows the CV analysis at various scan rates from 0.1 to 1 mV/s, where the energy storage kinetics of the SnO₂@G@C electrode and the Si-SnO₂@G@C electrode are further investigated. In consideration of the high rate capacity and great lithium ion diffusion, it can be inferred that pseudocapacitance may dominate the charge transfer during charge–discharge process. The charge storage can be analyzed according to the power-law relationship $i = k_1\nu^{1/2} + k_2\nu = a\nu^b$, where i and ν are the current and sweep rate, a and b are represented adjustable parameters, $k_1\nu^{1/2}$ is the diffusion-controlled contribution, and $k_2\nu$ is the capacitive contribution.⁴⁴ When the b value approaches 0.5, it is a diffusion-controlled lithium storage process. While it is near 1.0, the electrochemical reactions are dominated by the surface capacitance.⁴¹ Figure 8c,d exhibits the log(ν)–log(i) plots for the Si-SnO₂@G@C electrode and the SnO₂@G@C electrode to obtain the b value. The b values corresponding to the strongest reduction and oxidation peak currents of SnO₂@G@C and Si-SnO₂@G@C electrodes are fitted to be 0.83/0.89 and 0.81/0.90, respectively. It confirms the synergistic effect of the surface-controlled capacitive reaction and diffusion-controlled redox reaction. Note that the conversion process is capacitive-dominant and quite rapid. Besides, the b values of the oxidation peaks are closer to 1, indicating that the charge transfer is faster in the delithiation process. Furthermore, there is no significant difference in the b values of the two electrodes, which proves that the doped Si does not destroy the original lithium storage mechanism of the composite.

Consequently, the sandwich-architecture composite of Si-doped SnO₂ nanorods and reduced graphene oxide with C sealing (Si-SnO₂@G@C) shows improved electrochemical performance, as compared to the SnO₂@G, Si-SnO₂@G, and SnO₂@G@C, which is desirable for high capacity and long

cycle life span LIBs. Moreover, the lithium storage property of the Si-SnO₂@G@C electrode is in excess of most Sn-based anode materials because of the doped Si and the carbon sealing. The comparison of the rate and cycling performance of the Si-SnO₂@G@C electrode and that of the reported Sn-based anode materials in recent years is summarized in Figure 9 and Table 1, respectively. Based on the above discussion, the

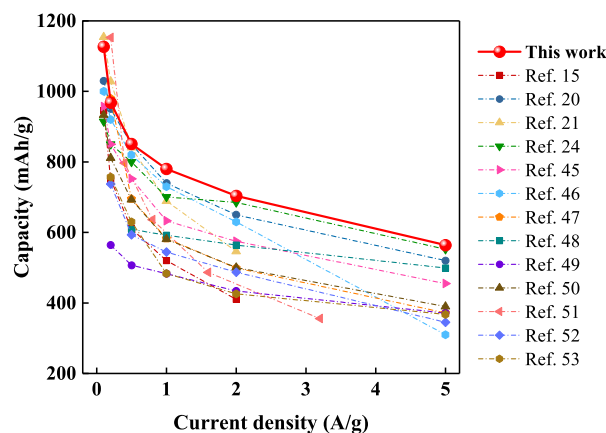


Figure 9. Rate performance comparison of the Si-SnO₂@G@C electrode and previously reported SnO₂-based anode materials.

Table 1. Comparison of Cycling Performance the Si-SnO₂@G@C Electrode and Previously Reported SnO₂-Based Anode Materials

SnO ₂ -based materials	rate (A/g)	capacity (mAh/g)	cycles (times)	year	ref
W-SnO ₂ @rGO	1	776	2000	2017	10
C-SnO ₂ @3D-CNT	1	452	500	2019	12
SnO ₂ /NSGS	2	480	2000	2018	16
C-graphene/SnO ₂	1	445	250	2018	18
SnO _{2-x} nanoparticles	2	700	1000	2017	19
SnO ₂ /Co@C	5	400	1800	2017	20
hollow SnO ₂ @GO	1	553	500	2017	21
SnO ₂ /GS	2	564	200	2018	24
SnO ₂ /Sn-rGO	1.6	449	400	2018	25
SnO ₂ @C	1	668	200	2017	35
C@SnO ₂ -rGO-SnO ₂	2	525	1200	2019	39
SnO ₂ @HPC@NC	1	767	500	2019	46
SnO ₂ /NC submicrobox	0.5	491	100	2016	47
h-SnO ₂ microspheres	5	404	600	2018	48
hollow SnO ₂ /N-rGO	1	652	200	2018	49
C/SnO ₂ /Sn	1	504	1000	2017	50
C@SnO ₂ @C	5	400	10000	2019	51
SnO ₂ /RGO	0.5	704	150	2019	52
SnO ₂ @C@VO ₂	0.5	597	100	2017	53
Si-SnO ₂ @G@C	0.5	772	200		this work
	2	654	1200		

excellent electrochemical performance could be attributed to the synergistic effect of the carbon coating and the doped Si in the following four ways. (1) The sandwich structure that the

C-coating tightly wraps the Si-doped SnO₂ nanorods on the surface of graphene can block the diffusion of Sn atoms and efficiently reduce the aggregation of Sn nanoparticles. The carbon layer also blocks the direct contact of the SnO₂ nanorods with electrolyte and prevents the graphene nanosheets from restacking, which can ensure the great cycling stability of the Si-SnO₂@G@C electrode. (2) The doped Si can make the structure more wrinkled and porous, providing more extra space for accommodating the volume variations and more active sites for reactions. Therefore, since extra lithium ions can be adsorbed in more wrinkled structures, the specific capacity of the electrode can be significantly increased. (3) The reversibility of lithiation/delithiation reactions is remarkably improved by the doped Si, which contributes to the initial Coulombic efficiency. (4) The doped Si not only generates Li⁺ conductive Li₄SiO₄ during lithiation process but also decreases the defects in the carbon matrix. It indeed accelerates the diffusion of Li⁺. As a result, the rate performance and the electrical conductivity are improved.

4. CONCLUSIONS

A sandwich-architecture composite of Si-doped SnO₂ nanorods and reduced graphene oxide with C sealing is fabricated by using a facile method of two-step hydrothermal reaction and subsequent thermal treatment, which improves the electrochemical performance of the SnO₂-based anode materials. In the porous sandwich structure, the Si-doped SnO₂ nanoparticles on the surface of graphene were firmly wrapped in the C-coating. It can efficiently prevent the Sn nanoparticles from aggregation and provide more extra space for accommodating the volume variations and more active sites for reactions. With the contribution of the synergistic effect of the carbon coating and the doped Si, the Si-SnO₂@G@C nanocomposite exhibits extraordinary rate performance, ultra-high specific capacity, excellent cycle stability, and high electrical conductivity as the anode of LIBs.

■ ASSOCIATED CONTENT

Supporting Information

The Supporting Information is available free of charge at <https://pubs.acs.org/doi/10.1021/acsami.0c00073>.

SEM and TEM images of SnO₂@G, SnO₂@G@C, Si-SnO₂@G, and Si-SnO₂@G@C, N₂ adsorption-desorption isotherms and BET surface area of SnO₂@G, SnO₂@G@C, and Si-SnO₂@G, XPS general spectra and high-resolution spectra for Sn 3d, O 1s, C 1s, and Si 2p regions of Si-SnO₂@G@C, rate performance of the composite electrodes with different silicon content at various current densities, the fitting values of R_e, R_p, and R_{ct} for the SnO₂@G@C and Si-SnO₂@G@C electrodes (PDF)

■ AUTHOR INFORMATION

Corresponding Author

Zhigao Hu – Technical Center for Multifunctional Magneto-Optical Spectroscopy (Shanghai), Engineering Research Center of Nanophotonics & Advanced Instrument (Ministry of Education), Department of Materials, School of Physics and Electronic Science, East China Normal University, Shanghai 200241, China; Collaborative Innovation Center of Extreme Optics, Shanxi University, Taiyuan, Shanxi 030006, China; Shanghai Institute of Intelligent Electronics & Systems, Fudan

University, Shanghai 200433, China; orcid.org/0000-0003-0575-2191; Phone: +86-21-54345150; Email: zghu@ee.ecnu.edu.cn; Fax: +86-21-54342933

<https://pubs.acs.org/10.1021/acsami.0c00073>

Authors

Liyuan Ao – Technical Center for Multifunctional Magneto-Optical Spectroscopy (Shanghai), Engineering Research Center of Nanophotonics & Advanced Instrument (Ministry of Education), Department of Materials, School of Physics and Electronic Science, East China Normal University, Shanghai 200241, China

Cong Wu – Technical Center for Multifunctional Magneto-Optical Spectroscopy (Shanghai), Engineering Research Center of Nanophotonics & Advanced Instrument (Ministry of Education), Department of Materials, School of Physics and Electronic Science, East China Normal University, Shanghai 200241, China

Xiang Wang – Technical Center for Multifunctional Magneto-Optical Spectroscopy (Shanghai), Engineering Research Center of Nanophotonics & Advanced Instrument (Ministry of Education), Department of Materials, School of Physics and Electronic Science, East China Normal University, Shanghai 200241, China

Yanan Xu – Technical Center for Multifunctional Magneto-Optical Spectroscopy (Shanghai), Engineering Research Center of Nanophotonics & Advanced Instrument (Ministry of Education), Department of Materials, School of Physics and Electronic Science, East China Normal University, Shanghai 200241, China

Kai Jiang – Technical Center for Multifunctional Magneto-Optical Spectroscopy (Shanghai), Engineering Research Center of Nanophotonics & Advanced Instrument (Ministry of Education), Department of Materials, School of Physics and Electronic Science, East China Normal University, Shanghai 200241, China

Liyan Shang – Technical Center for Multifunctional Magneto-Optical Spectroscopy (Shanghai), Engineering Research Center of Nanophotonics & Advanced Instrument (Ministry of Education), Department of Materials, School of Physics and Electronic Science, East China Normal University, Shanghai 200241, China

Yawei Li – Technical Center for Multifunctional Magneto-Optical Spectroscopy (Shanghai), Engineering Research Center of Nanophotonics & Advanced Instrument (Ministry of Education), Department of Materials, School of Physics and Electronic Science, East China Normal University, Shanghai 200241, China; orcid.org/0000-0001-8776-5687

Jinzhong Zhang – Technical Center for Multifunctional Magneto-Optical Spectroscopy (Shanghai), Engineering Research Center of Nanophotonics & Advanced Instrument (Ministry of Education), Department of Materials, School of Physics and Electronic Science, East China Normal University, Shanghai 200241, China

Junhao Chu – Technical Center for Multifunctional Magneto-Optical Spectroscopy (Shanghai), Engineering Research Center of Nanophotonics & Advanced Instrument (Ministry of Education), Department of Materials, School of Physics and Electronic Science, East China Normal University, Shanghai 200241, China; Collaborative Innovation Center of Extreme Optics, Shanxi University, Taiyuan, Shanxi 030006, China; Shanghai Institute of Intelligent Electronics & Systems, Fudan University, Shanghai 200433, China

Complete contact information is available at:

Notes

The authors declare no competing financial interest.

ACKNOWLEDGMENTS

This work was financially supported by the National Key Research and Development Program of China (Grants 2018YFB0406500, 2019YFB2203403, and 2017YFA0303403), the Natural Science Foundation of China (Grants 91833303, 61974043, and 61674057), Projects of Science and Technology Commission of Shanghai Municipality (Grants 18JC1412400, 18YF1407200, 18YF1407000, and 19511120100), and the Program for Professor of Special Appointment (Eastern Scholar) at Shanghai Institutions of Higher Learning and the Fundamental Research Funds for the Central Universities.

REFERENCES

- (1) Armand, M.; Tarascon, J. M. Building Better Batteries. *Nature* **2008**, *451*, 652–657.
- (2) Arico, A. S.; Bruce, P.; Scrosati, B.; Tarascon, J.-M.; van Schalkwijk, W. Nanostructured Materials for Advanced Energy Conversion and Storage Devices. *Nat. Mater.* **2005**, *4*, 366–377.
- (3) Chan, C. K.; Peng, H. L.; Liu, G.; McIlwrath, K.; Zhang, X. F.; Huggins, R. A.; Cui, Y. High-Performance Lithium Battery Anodes Using Silicon Nanowires. *Nat. Nanotechnol.* **2008**, *3*, 31.
- (4) Etacheri, V.; Marom, R.; Elazari, R.; Salitra, G.; Aurbach, D. Challenges in the Development of Advanced Li-ion Batteries: A Review. *Energy Environ. Sci.* **2011**, *4*, 3243–0.
- (5) Choi, J.; Aurbach, D. Promise and Reality of Post-Lithium-ion Batteries with High Energy Densities. *Nat. Rev. Mater.* **2016**, *1*, 16013.
- (6) Kim, T. H.; Park, J. S.; Chang, S. K.; Choi, S.; Ryu, J. H.; Song, H. K. The Current Move of Lithium Ion Batteries Towards the Next Phase. *Adv. Energy Mater.* **2012**, *2*, 860–872.
- (7) Chao, D.; Zhu, C.; Yang, P.; Xia, X.; Liu, J.; Wang, J.; Fan, X.; Savilov, S. V.; Lin, J.; Fan, H. J.; Shen, Z. X. Array of Nanosheets Render Ultrafast and High-Capacity Na-Ion Storage by Tunable Pseudocapacitance. *Nat. Commun.* **2016**, *7*, 12122.
- (8) Bhattacharya, P.; Kota, M.; Suh, D. H.; Roh, K. C.; Park, H. S. Biomimetic Spider-Web-Like Composites for Enhanced Rate Capability and Cycle Life of Lithium Ion Battery Anodes. *Adv. Energy Mater.* **2017**, *7*, 1700331.
- (9) Yun, S.; Bak, S. M.; Kim, S.; Yeon, J. S.; Kim, M. G.; Yang, X. Q.; Braun, P. V.; Park, H. S. Rational Design of Hierarchically Open-Porous Spherical Hybrid Architectures for Lithium-Ion Batteries. *Adv. Energy Mater.* **2019**, *9*, 1802816.
- (10) Wang, S.; Shi, L. Y.; Chen, G. R.; Ba, C. Q.; Wang, Z. Y.; Zhu, J. F.; Zhao, Y.; Zhang, M. H.; Yuan, S. In Situ Synthesis of Sungsten-Doped SnO₂ and Graphene Nanocomposites for High-Performance Anode Materials of Lithium-Ion Batteries. *ACS Appl. Mater. Interfaces* **2017**, *9*, 17163–17171.
- (11) Ren, W. H.; Liu, D. N.; Sun, C. L.; Yao, X. H.; Tan, J.; Wang, C. M.; Zhao, K. N.; Wang, X. P.; Li, Q.; Mai, L. Q. Nonhierarchical Heterostructured Fe₂O₃/Mn₂O₃ Porous Hollow Spheres for Enhanced Lithium Storage. *Small* **2018**, *14*, 1800659.
- (12) Bhattacharya, P.; Lee, J. H.; Kar, K. K.; Park, H. S. Carambola-shaped SnO₂ wrapped in carbon nanotube network for high volumetric capacity and improved rate and cycle stability of lithium ion battery. *Chem. Eng. J.* **2019**, *369*, 422–431.
- (13) Wang, H. J.; Jiang, X. Y.; Chai, Y.; Yang, X.; Yuan, R. Sandwich-Like C@SnO₂/Sn/Void@C Hollow Spheres as Improved Anode Materials for Lithium Ion Batteries. *J. Power Sources* **2018**, *379*, 191–196.
- (14) Jiang, Y.; Wan, Y. Y.; Jiang, W.; Tao, H. H.; Li, W. R.; Huang, S. S.; Chen, Z. W.; Zhao, B. Stabilizing the Reversible Capacity of SnO₂/

Graphene Composites by Cu Nanoparticles. *Chem. Eng. J.* **2019**, *367*, 45–54.

(15) Yang, L.; Dai, T.; Wang, Y. C.; Xie, D. G.; Narayan, R. L.; Li, J.; Ning, X. H. Chestnut-Like SnO₂/C Nanocomposites with Enhanced Lithium Ion Storage Properties. *Nano Energy* **2016**, *30*, 885–891.

(16) Wang, H. G.; Wu, Q.; Wang, Y. H.; Wang, X.; Wu, L. L.; Song, S. Y.; Zhang, H. J. Molecular Engineering of Monodisperse SnO₂ Nanocrystals Anchored on Doped Graphene with High-Performance Lithium/Sodium-Storage Properties in Half/Full Cells. *Adv. Energy Mater.* **2019**, *9*, 1802993.

(17) Han, J.; Kong, D.; Lv, W.; Tang, D. M.; Han, D.; Zhang, C.; Liu, D.; Xiao, Z.; Zhang, X.; Xiao, J.; He, X.; Hsia, F.; Zhang, C. C.; Tao, Y.; Golberg, D.; Kang, F.; Zhi, L.; Yang, Q. H. Caging Tin Oxide in Three-Dimensional Graphene Networks for Superior Volumetric Lithium Storage. *Nat. Commun.* **2018**, *9*, 402.

(18) Liu, X. H.; Ma, T. T.; Sun, L.; Xu, Y. S.; Zhang, J.; Pinna, N. Enhancing the Lithium Storage Performance of Graphene/SnO₂ Nanorods by a Carbon-Riveting Strategy. *ChemSusChem* **2018**, *11*, 1321–1327.

(19) Dong, W.; Xu, J.; Wang, C.; Lu, Y.; Liu, X.; Wang, X.; Yuan, X.; Wang, Z.; Lin, T.; Sui, M.; Chen, I. W.; Huang, F. A Robust and Conductive Black Tin Oxide Nanostructure Makes Efficient Lithium-Ion Batteries Possible. *Adv. Mater.* **2017**, *29*, 1700136.

(20) He, Q.; Liu, J.; Li, Z.; Li, Q.; Xu, L.; Zhang, B.; Meng, J.; Wu, Y.; Mai, L. Solvent-Free Synthesis of Uniform MOF Shell-Derived Carbon Confined SnO₂/Co Nanocubes for Highly Reversible Lithium Storage. *Small* **2017**, *13*, 1701504.

(21) Hu, X.; Zeng, G.; Chen, J. X.; Lu, C. Z.; Wen, Z. H. 3D Graphene Network Encapsulating SnO₂ Hollow Spheres as a High-Performance Anode Material for Lithium-Ion Batteries. *J. Mater. Chem. A* **2017**, *5*, 4535–4542.

(22) Chen, W. H.; Song, K. M.; Mi, L. W.; Feng, X. M.; Zhang, J. M.; Cui, S. Z.; Liu, C. T. Synergistic Effect Induced Ultrafine SnO₂/Graphene Nanocomposite as an Advanced Lithium/Sodium-Ion Batteries Anode. *J. Mater. Chem. A* **2017**, *5*, 10027–10038.

(23) Liu, D.; Kong, Z.; Liu, X.; Fu, A.; Wang, Y.; Guo, Y. G.; Guo, P.; Li, H.; Zhao, X. S. Spray-Drying-Induced Assembly of Skeleton-Structured SnO₂/Graphene Composite Spheres as Superior Anode Materials for High-Performance Lithium-Ion Batteries. *ACS Appl. Mater. Interfaces* **2018**, *10*, 2515–2525.

(24) Zhao, B.; Wang, Z.; Wang, S.; Jiang, J.; Si, J.; Huang, S.; Chen, Z.; Li, W.; Jiang, Y. Sandwiched Spherical Tin Dioxide/Graphene with a Three-Dimensional Interconnected Closed Pore Structure for Lithium Storage. *Nanoscale* **2018**, *10*, 16116–16126.

(25) Sui, X.; Huang, X.; Wu, Y.; Ren, R.; Pu, H.; Chang, J.; Zhou, G.; Mao, S.; Chen, J. Organometallic Precursor-Derived SnO₂/Sn-Reduced Graphene Oxide Sandwiched Nanocomposite Anode with Superior Lithium Storage Capacity. *ACS Appl. Mater. Interfaces* **2018**, *10*, 26170–26177.

(26) Han, Y.; Qi, P.; Zhou, J.; Feng, X.; Li, S.; Fu, X.; Zhao, J.; Yu, D.; Wang, B. Metal-Organic Frameworks (MOFs) as Sandwich Coating Cushion for Silicon Anode in Lithium Ion Batteries. *ACS Appl. Mater. Interfaces* **2015**, *7*, 26608–26613.

(27) Wu, J.; Liu, J.; Wang, Z.; Gong, X.; Wang, Y. A New Design for Si Wears Double Jackets Used as a High-Performance Lithium-Ion Battery Anode. *Chem. Eng. J.* **2019**, *370*, 565–572.

(28) Li, X. W.; Yang, Z. B.; Lin, S. M.; Li, D.; Yue, H. W.; Shang, X. N.; Fu, Y. J.; He, D. Y. A facile and Inexpensive Approach to Improve the Performance of Silicon Film as an Anode for Lithium Ion Batteries. *J. Mater. Chem. A* **2014**, *2*, 14817–14821.

(29) Liu, X. H.; Zhong, L.; Huang, S.; Mao, S. X.; Zhu, T.; Huang, J. Y. Size-Dependent Fracture of Silicon Nanoparticles During Lithiation. *ACS Nano* **2012**, *6*, 1522–1531.

(30) Zhou, Z. W.; Liu, Y. T.; Xie, X. M.; Ye, X. Y. Constructing Novel Si@SnO₂ Core/Shell Heterostructures by Facile Self-Assembly of SnO₂ Nanowires on Silicon Hollow Nanospheres for Large, Reversible Lithium Storage. *ACS Appl. Mater. Interfaces* **2016**, *8*, 7092–7100.

(31) Ma, T. Y.; Yu, X. N.; Li, H. Y.; Zhang, W. G.; Cheng, X. L.; Zhu, W. T.; Qiu, X. P. High Volumetric Capacity of Hollow Structured SnO₂@Si Nanospheres for Lithium-Ion Batteries. *Nano Lett.* **2017**, *17*, 3959–3964.

(32) He, H. Y.; Fu, W.; Wang, H. T.; Wang, H.; Jin, C. H.; Fan, H. J.; Liu, Z. Silica-Modified SnO₂-Graphene “Slime” for Self-Enhanced Li-Ion Battery Anode. *Nano Energy* **2017**, *34*, 449–455.

(33) Chi, C.; Lan, J.; Sun, J.; Liu, Y.; Yu, Y.; Yang, X. A Facile Electrospinning and Electrospinning Synchronization Technique for Preparation of High Performance MnO/C@rGO Composite Anodes for Lithium Storage. *RSC Adv.* **2015**, *5*, 41210–41217.

(34) Shi, L.; Wang, W. K.; Wang, A. B.; Yuan, K. G.; Jin, Z. Q.; Yang, Y. S. Scalable Synthesis of Core-Shell Structured SiO_x/Nitrogen-Doped Carbon Composite as a High-Performance Anode Material for Lithium-Ion Batteries. *J. Power Sources* **2016**, *318*, 184–191.

(35) Wang, X. W.; Zhang, L. D.; Zhang, C. C.; Wu, P. Y. Mesoporous Graphene/Carbon Framework Embedded with SnO₂ Nanoparticles as a Highperformance Anode for Lithium Storage. *Inorg. Chem. Front.* **2017**, *4*, 889–897.

(36) Schneider, P. Adsorption Isotherms of Microporous-Mesoporous Solids Revisited. *Appl. Catal., A* **1995**, *129*, 157–165.

(37) Zhu, C.; Xia, X.; Liu, J.; Fan, Z.; Chao, D.; Zhang, H.; Fan, H. J. TiO₂ Nanotube@SnO₂ Nanoflake Core-Branch Arrays for Lithium-Ion Battery Anode. *Nano Energy* **2014**, *4*, 105–112.

(38) Tan, Y.; Wong, K. W.; Ng, K. M. Novel Silicon Doped Tin Oxide-Carbon Microspheres as Anode Material for Lithium Ion Batteries: The Multiple Effects Exerted by Doped Si. *Small* **2017**, *13*, 1702614.

(39) Yao, W. Q.; Wu, S. B.; Zhan, L.; Wang, Y. L. Two-Dimensional Porous Carbon-Coated Sandwich-Like Mesoporous SnO₂/Graphene/Mesoporous SnO₂ Nanosheets towards High-Rate and Long Cycle Life Lithium-Ion Batteries. *Chem. Eng. J.* **2019**, *361*, 329–341.

(40) Li, Z.; Zhao, H.; Lv, P.; Zhang, Z.; Zhang, Y.; Du, Z.; Teng, Y.; Zhao, L.; Zhu, Z. Watermelon-Like Structured SiO_x-TiO₂@C Nanocomposite as a High-Performance Lithium-Ion Battery Anode. *Adv. Funct. Mater.* **2018**, *28*, 1605711.

(41) Wang, J. Y.; Wu, C.; Deng, Q. L.; Jiang, K.; Shang, L. Y.; Hu, Z. G.; Chu, J. H. Highly Durable and Cycle-Stable Lithium Storage Based on MnO Nanoparticle-Decorated 3D Interconnected CNT/Graphene Architecture. *Nanoscale* **2018**, *10*, 13140–13148.

(42) Ao, X.; Jiang, J.; Ruan, Y.; Li, Z.; Zhang, Y.; Sun, J.; Wang, C. Honeycomb-inspired Design of Ultrafine SnO₂@C Nanospheres Embedded in Carbon Film as Anode Materials for High Performance Lithium- and Sodium-Ion Battery. *J. Power Sources* **2017**, *359*, 340–348.

(43) Chen, Y.; Ge, D.; Zhang, J.; Chu, R.; Zheng, J.; Wu, C.; Zeng, Y.; Zhang, Y.; Guo, H. Ultrafine Mo-doped SnO₂ Nanostructure and Derivative Mo-Doped Sn/C Nanofibers for High-Performance Lithium-Ion Batteries. *Nanoscale* **2018**, *10*, 17378–17387.

(44) Li, M. J.; Deng, Q. L.; Wang, J. Y.; Jiang, K.; Hu, Z. G.; Chu, J. H. In Situ Carbon Encapsulation of Vertical MoS₂ Arrays with SnO₂ for Durable High Rate Lithium Storage: Dominant Pseudocapacitive Behavior. *Nanoscale* **2018**, *10*, 741–751.

(45) Wang, Z. X.; Song, D. Y.; Si, J.; Jiang, Y.; Yang, Y. Q.; Jiang, Y.; Huang, S. S.; Chen, Z. W.; Zhao, B. One-Step Hydrothermal Reduction Synthesis of Tiny Sn/SnO₂ Nanoparticles Sandwiching Between Spherical Graphene with Excellent Lithium Storage Cycling Performances. *Electrochim. Acta* **2018**, *292*, 72–80.

(46) Hong, Y.; Mao, W. F.; Hu, Q. Q.; Chang, S. Y.; Li, D. J.; Zhang, J. B.; Liu, G.; Ai, G. Nitrogen-Doped Carbon Coated SnO₂ Nanoparticles Embedded in a Hierarchical Porous Carbon Framework for High-Performance Lithium-Ion Battery Anodes. *J. Power Sources* **2019**, *428*, 44–52.

(47) Zhou, X. S.; Yu, L.; Lou, X. W. Formation of Uniform N-doped Carbon-Coated SnO₂ Submicroboxes with Enhanced Lithium Storage Properties. *Adv. Energy Mater.* **2016**, *6*, 1600451.

(48) Park, G. D.; Kang, Y. C. Rational Design and Synthesis of Hierarchically Structured SnO₂ Microspheres Assembled from

Hollow Porous Nanoplates as Superior Anode Materials for Lithium-Ion Batteries. *Nano Res.* **2018**, *11*, 1301–1312.

(49) Wu, N.; Du, W.; Gao, X.; Zhao, L.; Liu, G.; Liu, X.; Wu, H.; He, Y. B. Hollow SnO₂ Nanospheres with Oxygen Vacancies Entrapped by a N-doped Graphene Network as Robust Anode Materials for Lithium-ion Batteries. *Nanoscale* **2018**, *10*, 11460–11466.

(50) Cheng, Y.; Yi, Z.; Wang, C.; Wu, Y.; Wang, L. Controllable fabrication of C/Sn and C/SnO/Sn composites as anode materials for high-performance lithium-ion batteries. *Chem. Eng. J.* **2017**, *330*, 1035–1043.

(51) Cao, B.; Liu, Z.; Xu, C.; Huang, J.; Fang, H.; Chen, Y. High-Rate-Induced Capacity Evolution of Mesoporous C@SnO₂@C Hollow Nanospheres for Ultra-Long Cycle Lithium-Ion Batteries. *J. Power Sources* **2019**, *414*, 233–241.

(52) Tan, Q.; Kong, Z.; Chen, X.; Zhang, L.; Hu, X.; Mu, M.; Sun, H.; Shao, X.; Guan, X.; Gao, M.; Xu, B. Synthesis of SnO₂/Graphene Composite Anode Materials for Lithium-Ion Batteries. *Appl. Surf. Sci.* **2019**, *485*, 314–322.

(53) Guo, W.; Wang, Y.; Li, Q.; Wang, D.; Zhang, F.; Yang, Y.; Yu, Y. SnO₂@C@VO₂ Composite Hollow Nanospheres as an Anode Material for Lithium-Ion Batteries. *ACS Appl. Mater. Interfaces* **2018**, *10*, 14993–15000.